Quantitative phase and absorption tomography with an X-ray grating interferometer and synchrotron radiation

I. Zanette*,1, T. Weitkamp2, S. Lang3, M. Langer1,4, J. Mohr5, C. David6, and J. Baruchel1

[1] European Synchrotron Radiation Facility, Grenoble, France
[2] Synchrotron Soleil, Gif-sur-Yvette, France
[3] Biomaterials Science Center, University of Basel, Basel, Switzerland
[4] Université de Lyon, CREATIS-LRMN, CNRS UMR5220, Inserm U630, INSA-Lyon, Université Lyon 1, Villeurbanne, France
[5] Institute for Microstructure Technology, Karlsruhe Institute of Technology, Karlsruhe, Germany
[6] Laboratory for Micro- and Nanotechnology, Paul Scherrer Institut, Villigen, Switzerland

* Corresponding author: e-mail **irene.zanette@esrf.fr**, Phone: +33-(0)4-76881750, Fax: +33-(0)4-76882252

We report on a study on the accuracy and precision of X-ray phase and absorption tomograms obtained with a grating interferometer using monochromatic synchrotron radiation. The quantitative assessment of the performances of the X-ray interferometer is a fundamental aspect in the interpretation of the results obtained with this device. The work presented in this paper consists in the comparison of experimental with calculated three-dimensional distributions of the X-ray refractive index in a phantom sample made of known materials. The quality of phase and absorption tomograms has been determined with respect to their sensitivity and contrast-to-noise ratios. Moreover, the effect of image artifacts typical in phase contrast imaging based on the phase-stepping technique, especially stripe features generated by the phase wrapping phenomenon, has been investigated by comparison with numerical simulations. The results show that the artifacts cannot only be qualitatively explained by the calculations, but they can even be quantitatively reproduced.

1 Introduction Conventional X-ray radiography, in which contrast is obtained from the absorption of the X-rays in the specimen under study, finds its limitation when details with similar densities need to be discriminated. For example, inner structures in soft-tissue biological specimens are imaged with poor contrast in conventional absorption X-ray imaging.

Phase-contrast X-ray imaging overcomes this limitation by using the phase shift rather than the absorption as the image signal [1]. In the hard X-ray range, this approach can be several orders of magnitude more sensitive than absorption contrast [2]. Among the different phase-contrast imaging techniques, a method based on an X-ray grating interferometer [3, 4] provides high-sensitivity phase-contrast images with high resolution. This method has been developed at synchrotron facilities and can be adapted to laboratory X-ray sources [5].

The phase and absorption tomographies obtained with the grating interferometer yield the three-dimensional (3D) distribution of the refractive index $n = 1 - \delta + i\beta$ of the object under study. In particular, δ is retrieved in the phase tomogram and β is reconstructed in the absorption tomogram. The correctness of the quantitative information retrieved in the phase and absorption tomograms is a fundamental aspect in the interpretation of the results given by the X-ray grating interferometer.

The aim of the work reported in this paper is to assess, through comparison of experimental results with calculated data, the quantitativeness of the refractive index measurements obtained with a grating interferometer, and monochromatic synchrotron radiation.

A phantom made of known materials was built for this study and was measured with the grating interferometer installed at the beamline ID19 of the European Synchrotron Radiation Facility (ESRF, France) [6, 7].

This work, performed with monochromatic synchrotron radiation, complements previous studies performed with Talbot–Lau interferometers on low-brilliance sources [8, 9].

Phys. Status Solidi A **208**, No. 11 (2011)

2527

Original

Paper

2 The X-ray grating interferometer An X-ray grating interferometer consists of two line gratings placed in the X-ray path between the sample and the detector (see Fig. 1). The first grating G1, the "beam-splitter," is a phase shifting grating which produces an interference pattern of quasi-periodic lines at particular distances D corresponding to fractional Talbot orders [10]. The interference pattern, whose period p is typically much smaller than the pixel size of the detector, contains information on the optical properties of the sample. The absorbing grating G2, the "analyzer grating," is positioned directly before the detector to analyze the interference pattern. The period p of the absorbing grating is the same as the period of the interference pattern.

In order to maintain the full spatial resolution of the imaging system, the analysis of the interference pattern is performed with the phase stepping technique. One of the two gratings is scanned perpendicular to the grating lines and the optical axis over at least one grating period and a series of images is recorded during the scan. The analysis of these images yields pseudo-absorption and refraction angle radiographs [10].

The "pseudo-absorption" radiographs are obtained by averaging all images recorded in the phase-stepping scan. They exhibit absorption contrast and, possibly, edge-enhancing in-line phase contrast. The presence of the in-line phase contrast in the pseudo-absorption images depends on the coherence properties of the radiation and on the sample-to-detector distance. The pseudo-absorption images are very similar to the conventional images that would be obtained if the interferometer were not in the beam, especially when the shearing distance between the two beams diffracted by G1 is small compared to the detector pixel size.

Where the edge-enhancement effect is not present, the quantity $T(x, y)$ measured in the absorption radiographs is a function of the line integral of the linear attenuation coefficient $\mu(x, y, z)$ of the sample:

$$T(x, y) = \exp\left[-\int \mu(x, y, z)\mathrm{d}z\right], \qquad (1)$$

where $\mu(x, y, z) = 4\pi\beta(x, y, z)/\lambda$ and λ is the wavelength of the radiation.

The signal recorded in the differential phase radiographs is related to the refraction angle α in the direction perpendicular to the grating lines. The deflection angle is proportional to the differential phase of the wave front $\partial\Phi(x, y)/\partial x$ along x and is related to the integral of the real part of the refractive index along the propagation direction [10]:

$$\alpha(x, y) = \frac{\lambda}{2\pi} \frac{\partial\Phi(x, y)}{\partial x} = \int \frac{\partial\delta(x, y, z)}{\partial x} \mathrm{d}z. \qquad (2)$$

The refraction of the X-rays from the sample causes a lateral displacement d of the interference pattern produced by G1, see Fig. 1. For small refraction angles, the displacement d is related to the angle α by

$$d \simeq \alpha D. \qquad (3)$$

The displacement d is measured by extracting, for each pixel, the phase ϕ of the intensity oscillation measured during the phase-stepping scan. (The oscillation phase ϕ should not be confused with the phase Φ of the wavefront.) The phase ϕ_s measured when the sample is in the beam is corrected for the reference phase ϕ_r by subtraction. If p is the
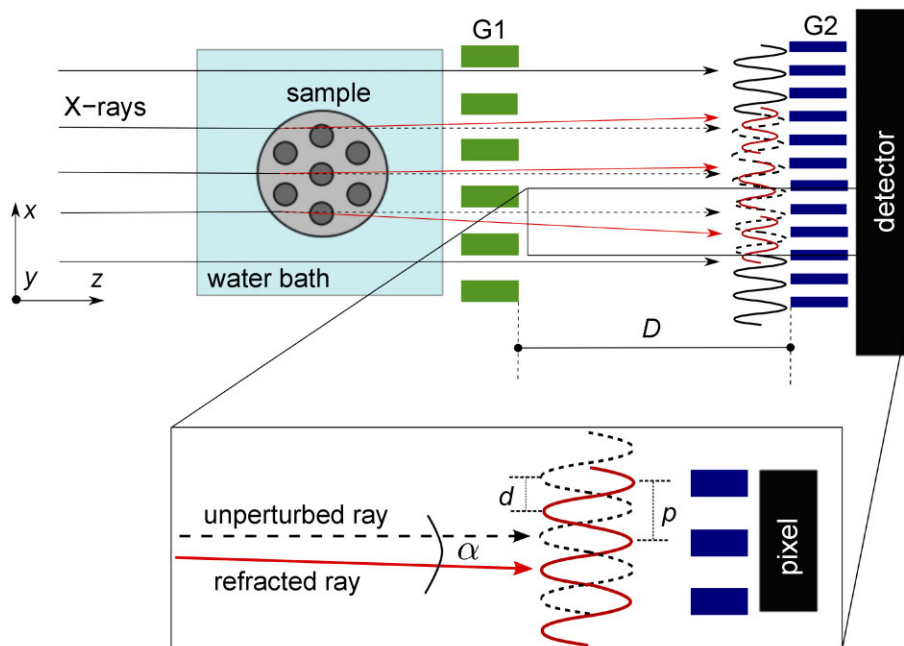
Figure 1 (online color at: www.pss-a.com) Top: schematic representation of an X-ray grating interferometer. The two gratings (G1 and G2) are usually placed between the sample and the detector, the distance D between the gratings corresponds to a fractional Talbot order. During the phase-stepping scan, the grating G1 is moved parallel to the x-axis. In a tomography scan, this procedure is repeated for hundreds of different viewing angles of the sample, which rotates around the y-axis. Below: detail showing the displacement d of the interference pattern, caused by the refraction in the sample. The refraction angle is indicated with α and p is the period of the interference pattern. The detector pixel size is usually larger than p and the analyzer grating is needed to analyze the interference pattern.

period of the interference pattern, d is given by

$$d = p\frac{\Delta\phi}{2\pi}, \tag{4}$$

where $\Delta\phi = \phi_s - \phi_r$. The phase ϕ can be measured in the interval $[-\pi, \pi]$. When the phase is outside this interval, the measurement of the phase difference $\Delta\phi$ and therefore the measurement of α are subject to errors. We discuss in detail the effect of the phase-wrapping phenomenon in Section 4.1.

The combination of phase stepping with tomography yields the 3D distribution of the full complex-valued index of refraction $n(x, y, z)$ of the specimen. Tomographic reconstruction of the pseudo-absorption images yields the 3D distribution of the linear attenuation coefficient $\mu(x, y, z)$ which is proportional to the imaginary part of the refractive index $\beta(x, y, z)$ (plus, possibly, some propagation-based edge enhancement). The absorption tomogram is usually obtained with the filtered backprojection (FBP) algorithm and a ramp filter. The FBP with an imaginary sign filter [11] applied to the refraction angle projections yields the 3D distribution of the decrement of the refractive index $\delta(x, y, z)$, henceforward referred to as "phase reconstruction."

3 Experimental parameters A grating interferometer [6] of the type described in the previous section and installed at beamline ID19 [7] of the ESRF has been used to measure the refractive index of a reference sample made of known materials arranged in a systematic geometry.

The measurements were made with 35-keV X-rays from a Si (111) double crystal monochromator. The sample was positioned at 150 m from the wiggler source. The grating G1 was situated 100 mm downstream of the sample, which was immersed in a tank filled with water in order to avoid artifacts from the refraction at the interface sample/air. The interferometer was operating at the fifth fractional Talbot order, the distance between G1 and G2 was 405 mm. The detector, a scintillator/lens-coupled Frelon CCD camera with 2048×2048 pixels and an effective pixel size of

8.12 µm, was positioned 50 mm downstream of G2. The beam-splitter with π-shifting Si lines had a period of 4.787 µm [12]. The gold lines of G2 had a period of 2.4 µm and a height of approximately 50 µm [13]. Phase-stepping scans were performed at 1500 evenly spaced angles over $360°$. Each phase-stepping scan was performed in four steps over one period of G2. The exposure time per image was 1.5 s.

The phantom was a polymethyl methacrylate (PMMA) cylinder of 8 mm diameter with seven cylindrical cavities of 0.8 mm diameter. The cavities were filled with different materials: five cavities contained solutions of dipotassium hydrogen phosphate (K_2HPO_4) in different concentrations, one contained pure water, and one was left empty. A wire of Al 99.99% of 125 µm diameter was added at the outer wall of the PMMA cylinder.

Table 1 shows the expected values μ_c and δ_c of, respectively, linear attenuation coefficient and decrement of the refractive index of the materials of the phantom. They have been calculated with the software XOP [14]. The XCOM database was used for the calculation of the linear attenuation coefficient and the Windt database was used for the calculation of decrement of refractive index. The linear attenuation coefficient μ_c takes into account both absorption and scattering effects.

4 Results and discussion The pseudo-absorption and phase reconstructions of a slice of the phantom are shown, respectively, in Fig. 2(a) and (b).

The numbers in the phase slice indicate the different materials reported in Table 1. The gray levels of the images in Fig. 2(a) and (b) are the difference of the linear attenuation coefficient $\Delta\mu = \mu - \mu^{H_2O}$ and of the decrement of refractive index $\Delta\delta = \delta - \delta^{H_2O}$ relative to water, respectively. They have been obtained by subtracting the average value of the gray levels measured in the capillary occupied by demineralized water.

In the phase slice [Fig. 2(b)], the PMMA cylinder can be distinguished from the surrounding water and all the discs

Table 1 Densities, linear attenuation coefficient, and real part of the refractive index of the materials in the phantom.

#	material description	density (g/cm³)	μ_c (cm^{-1})	δ_c (10^{-7})
1	air	0.00	0.000	0.002
2	PMMA	1.19	0.310	2.155
3	H_2O	1.00	0.307	1.881
4	K_2HPO_4 (50 mg/ml)	1.045 ± 0.004	0.369 ± 0.001	1.945 ± 0.008
5	K_2HPO_4 (100 mg/ml)	1.086 ± 0.004	0.429 ± 0.002	2.006 ± 0.008
6	K_2HPO_4 (200 mg/ml)	1.161 ± 0.005	0.550 ± 0.002	2.143 ± 0.009
7	K_2HPO_4 (300 mg/ml)	1.232 ± 0.005	0.662 ± 0.003	2.253 ± 0.009
8	K_2HPO_4 (700 mg/ml)	1.504 ± 0.006	1.081 ± 0.004	2.698 ± 0.011
9	Al	2.70	2.079	4.413

The solutions of K_2HPO_4 are described with the concentration of the salt in water. The densities of the solutions have been determined by weighing a known volume (25 ml in a calibrated flask) with a high-precision scale. The error associated to the densities measured in this way is 0.4%. Since both the linear attenuation coefficient and the decrement of refractive index are proportional to the mass density of the material, the same error of 0.4% is associated to the μ_c and δ_c values of the solutions. The other densities reported in the table are tabulated values in XOP.

| Original |
| Paper |

Phys. Status Solidi A **208**, No. 11 (2011) 2529
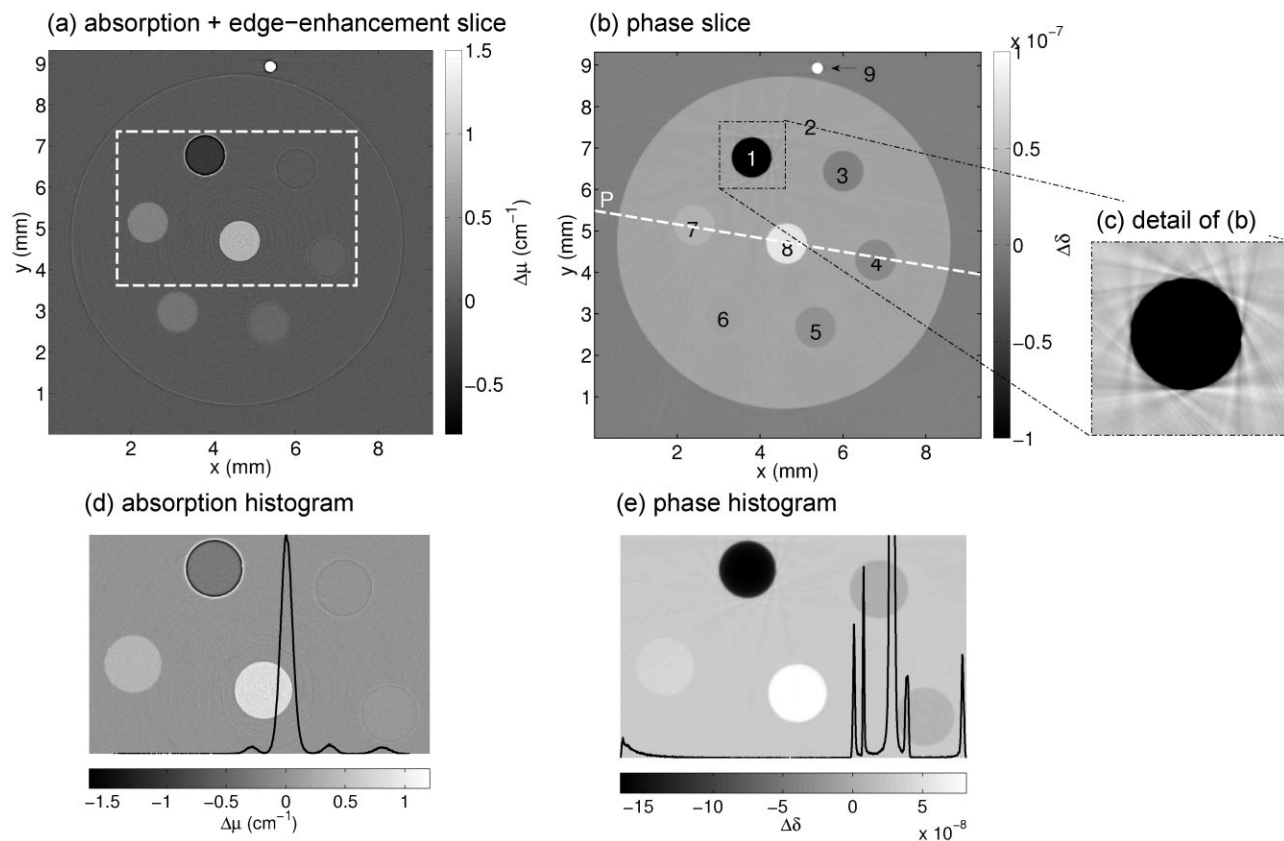
Figure 2 Absorption and edge-enhancement (a) and phase (b) tomographic reconstructions of the phantom used in this study. (c) Detail of (b) showing the image artifacts coming from the phase-wrapping effect. (d) Absorption and (e) phase histograms of the ROI indicated by a white dashed rectangle in panel (a). The y-axis of the phase histogram has been cut to one eleventh of the height of the peak corresponding to the PMMA in order to better visualize the other, smaller peaks.

can be discerned from the PMMA cylinder. The two materials that show the weakest contrast are solutions 6 and 7. On the other hand, these liquids can be clearly seen in the pseudo-absorption slice, Fig. 2(a). Here, however, materials 2–4 cannot be distinguished. Furthermore, in the absorption slice, the PMMA cylinder and materials 3 and 4 are only visible through edge enhancement. This phenomenon helps to identify interfaces but, in the general case of an inhomogeneous specimen, does not give quantitative information and its detectability will generally depend critically on the spatial resolution of the detector.

More information on the image signals can be obtained with histogram analysis. Figures 2(d) and (e) show, respectively, pseudo-absorption and phase histograms of the region-of-interest (ROI) of 715 pixels $\times$ 460 pixels delimited by a white dashed rectangle in Fig. 2(a). The selected ROI is also shown in the background of the histogram plots. The y-axis of the histograms represents the frequency of appearance of the gray levels in the ROI.

In the histogram of the absorption-contrast data, Fig. 2(d), only four peaks are present while in that of the phase tomogram [Fig. 2(e)] each of the six materials of the ROI forms a distinct peak. This shows the higher sensitivity of phase contrast compared to absorption contrast in

discerning the materials in the ROI. As already discussed, materials 2–4, whose gray levels are part of the same peak, cannot be separated in the absorption slice.

Note that all the peaks of the phase histogram except the peak corresponding to the PMMA are asymmetric: they have a tail towards the PMMA peak. We believe that the asymmetry in the histogram peaks is mainly due to the stripe artifacts generated around the capillary containing air [see also detail in Fig. 2(c)]. We explain the origin of these artifacts in the next section.

4.1 Phase wrapping In the phase slice of Fig. 2(b) stripe artifacts departing tangentially from the capillary containing air spread throughout the entire slice. A zoom of this capillary is shown in Fig. 2(c) where the contrast has been adjusted in order to highlight these artifacts. The same type of artifacts can be observed around the Al wire. In the following we show that these artifacts are caused by the phase wrapping effect introduced in Section 2.

Figure 3 shows the sinogram of $\Delta\phi$ values (Eq. (4)) from which the phase slice of Fig. 2(b) has been reconstructed. The zoomed insets in Fig. 3 are examples of wrapped parts of the sinogram: the parts causing the stripe artifacts of Fig. 2(b).

(a) experimental sinogram

(b) simulated slice - not wrapped (c) simulated slice - wrapped
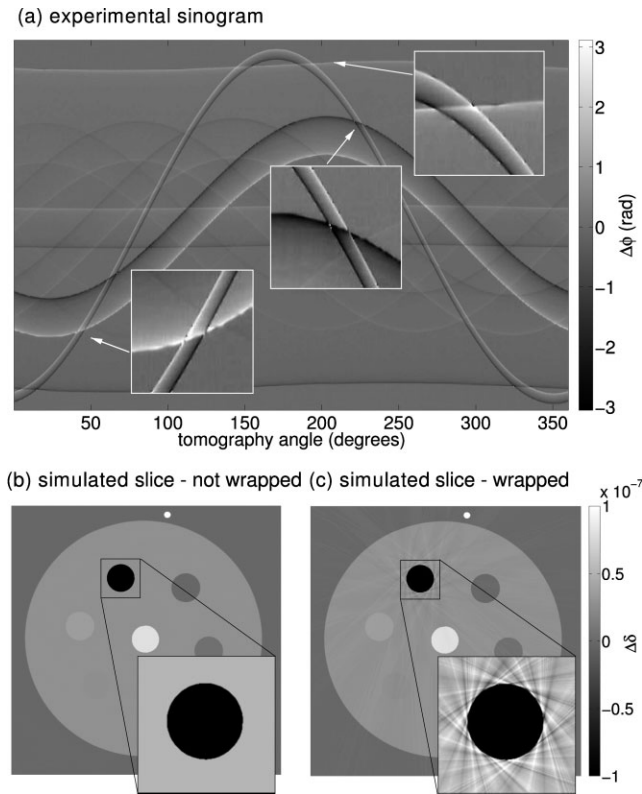
Figure 3 (a) Experimental sinogram of $\Delta\phi$ values; the insets show examples of wrapped parts. (b) Phase slice from ideal, noise-free sinogram of $\Delta\phi$, not wrapped. (c) Phase slice from ideal, noise-free sinogram in which $\Delta\phi$ is wrapped.

Simple one-dimensional phase unwrapping algorithms and path-following two-dimensional phase unwrapping algorithms [15] have been tested on our dataset but failed to unwrap it. Here, we prove, by comparison of numerical simulation with the experimental data, that the stripe artifacts of Fig. 2(b) are actually caused by the phase wrapping effect and not by anything else.

By segmenting the phase slice of Fig. 2(b), we obtained the ideal (noise free) phase slice of the phantom and we

generated from it the corresponding $\Delta\phi$ sinogram. In order to calculate the $\Delta\phi$ sinogram from the δ values, we used the relations reported in Eqs. ((2)–(4)). The sinogram computed in this way is a non-wrapped sinogram whose reconstruction gives a phase tomogram free of artifacts, as shown in Fig. 3(b). If, however, we wrap the ideal sinogram into the interval $[-\pi, \pi)$, the resulting tomographic phase reconstruction [Fig. 3(c)] shows artifacts that are not only of the same type as those observed in the experimental data (Fig. 2) but also show a very similar geometric structure. This geometry is given by the positions in the sinogram at which phase wrapping occurs. In the following quantitative analysis we will see how these errors affect the precision of the reconstructed values of the real part of the refractive index.
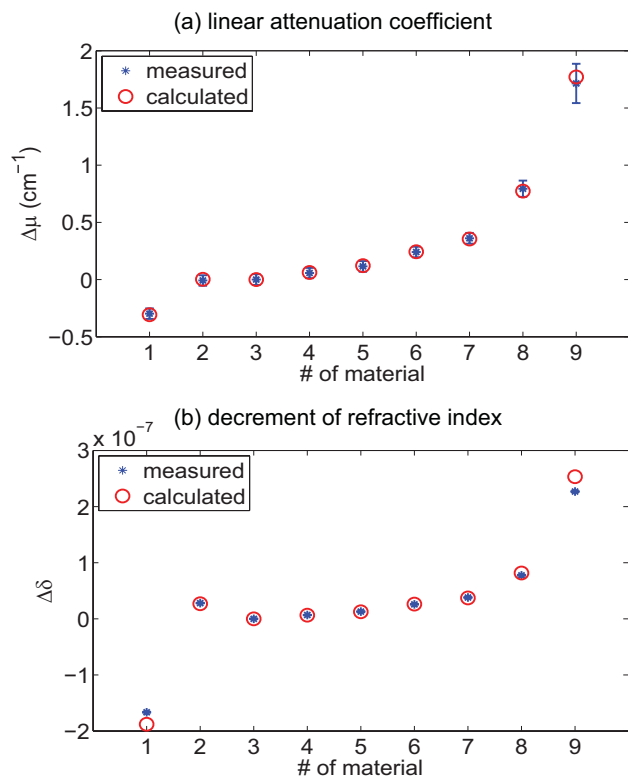
4.2 Quantitative comparison of δ and μ values, sensitivity, and contrast-to-noise ratio measurements The measured values of $\Delta\mu$ and $\Delta\delta$ extracted from the slices of Fig. 2 have been compared with the quantities $\Delta\mu_c = \mu_c - \mu_c^{H_2O}$ and $\Delta\delta_c = \delta_c - \delta_c^{H_2O}$ calculated from the numbers in Table 1 and reported in Table 2.

The measured values have been obtained by averaging the gray levels in circular ROIs each corresponding to one material in the tomographic slice. The area of the ROIs was of 3848 pixels, with the exception of the Al (314 pixels). The mean values $\overline{\Delta\mu}$ and $\overline{\Delta\delta}$ calculated in this way are reported in Table 2. The errors associated to these measurements, the standard deviation of the gray values in the ROIs, are displayed with error bars in Fig. 4(a) and (b) and listed in Table 2.

The measured linear attenuation coefficients match, within the error limits, with the calculated data. The decrements of refractive index are, in general, in good agreement with the calculated data. The biggest discrepancies between calculated and measured values are observed for air and Al (materials 1 and 9). They can, at least partly, be attributed to the phase wrapping phenomenon, as can be deduced from inspection of the simulated data. For example, the $\Delta\delta$ value measured in the air disc of the simulated slice shown in Fig. 3(c) is also underestimated with respect to the

Table 2 Comparison between calculated (subscript c) and experimental values of the linear attenuation coefficient and decrement of refractive index. The standard deviations associated to the measured values are also reported in the table.

#	material description	calculated $\Delta\mu_c$ (cm^{-1})	experim. $\overline{\Delta\mu}$ (cm^{-1})	std. dev. $\sigma_{\Delta\mu}$ (cm^{-1})	calculated $\Delta\delta_c$ (10^{-7})	experim. $\overline{\Delta\delta}$ (10^{-7})	std. dev. $\sigma_{\Delta\delta}$ (10^{-7})
1	air	-0.307	-0.297	0.046	-1.879	-1.666	0.037
2	PMMA	0.002	-0.007	0.046	0.268	0.269	0.007
3	H$_2$O	0.000	0.000	0.046	0.000	0.000	0.005
4	K$_2$HPO$_4$ (50 mg/ml)	0.062 ± 0.001	0.058	0.045	0.064 ± 0.008	0.067	0.004
5	K$_2$HPO$_4$ (100 mg/ml)	0.122 ± 0.002	0.116	0.047	0.124 ± 0.008	0.128	0.004
6	K$_2$HPO$_4$ (200 mg/ml)	0.243 ± 0.002	0.241	0.046	0.262 ± 0.009	0.257	0.005
7	K$_2$HPO$_4$ (300 mg/ml)	0.354 ± 0.003	0.362	0.047	0.372 ± 0.009	0.380	0.008
8	K$_2$HPO$_4$ (700 mg/ml)	0.774 ± 0.004	0.795	0.067	0.816 ± 0.011	0.775	0.007
9	Al	1.771	1.727	0.172	2.532	2.268	0.086

Original

Paper

Phys. Status Solidi A **208**, No. 11 (2011)

2531

(a) linear attenuation coefficient

(b) decrement of refractive index

Figure 4 (online color at: www.pss-a.com) Measurements of $\Delta\mu$ (a) and $\Delta\delta$ (b) extracted from slices in Fig. 2 and compared with the calculated values reported in Table 1.

Table 3 Absorption and phase contrast-to-noise ratios calculated with the formula in Eq. (5).

#	material description	CNR μ	CNR δ
1	air	4.5	338.0
2	PMMA	0.1	58.8
3	H_2O	0.2	3.5
4	K_2HPO_4 (50 mg/ml)	1.1	17.7
5	K_2HPO_4 (100 mg/ml)	2.0	30.4
6	K_2HPO_4 (200 mg/ml)	4.0	57.9
7	K_2HPO_4 (300 mg/ml)	5.9	82.4
8	K_2HPO_4 (700 mg/ml)	12.9	165.3
9	Al	27.5	460.1

Herzen et al. [8], using a polychromatic beam produced by a laboratory X-ray generator, obtained a higher value for the standard deviation of the background, corresponding to 4.9×10^{-10}. The experiment reported in Ref. [8] was performed at 28 keV mean energy, with the interferometer operating at the fifth fractional Talbot distance.
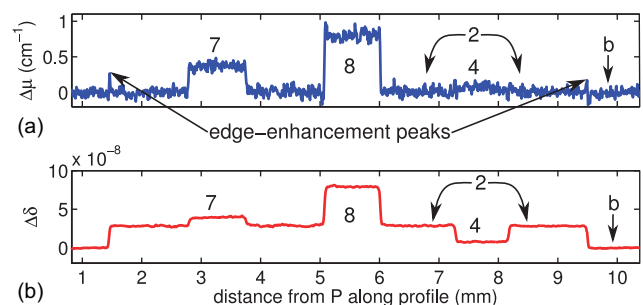
The standard deviation σ_b measured in a ROI of the image background together with the mean value of the ROI, $S_b = 2.8 \times 10^{-10}$, enters in the calculation of the contrast-to-noise ratio (CNR) of the different materials in the phase and absorption tomographies:

$$\mathrm{CNR}_x = \frac{|S_x - S_b|}{\sqrt{(\sigma_x^2 + \sigma_b^2)}}, \tag{5}$$

where the subscripts x and b refer to the material and the background, respectively. The values S_x and σ_x are the ones reported in Table 2.

Table 3 gives a list of the CNR values for δ and μ. Contrary to the results reported in Ref. [8], obtained with a polychromatic source, we have observed that the CNR in the phase slice is always substantially better than the CNR of the linear attenuation coefficient.

The higher CNR in the phase image compared to the CNR obtained in the absorption tomogram becomes evident in the section profiles of tomographic slices, shown in Fig. 5. The position at which the profiles have been extracted is

theoretical value and equal to -1.805×10^{-7}. While the discrepancy to the expected value is inferior than in the experimental data, it is clearly significant.

Another, smaller discrepancy is observed for the highest concentration of K_2HPO_4 (material number 8) probably due to the fact that the solution was saturated. This discrepancy can be detected in the phase slice due to the high sensitivity of the phase signal.

A figure of merit commonly used to assess the sensitivity of phase-contrast images provided by an X-ray grating interferometer is the standard deviation of the gray level values in a uniform region in the background of the phase reconstruction [8, 11, 16]. In the data presented here, the standard deviation of a ROI with an area of 3848 pixels extracted from a region of the phase slice occupied by water outside of the PMMA cylinder is 3.4×10^{-10}. This value, which is affected by several factors such as photon statistics, visibility of the interference pattern, presence of image artifacts, and size of the ROI, is slightly larger than other sensitivity measurements performed at ID19: Pfeiffer et al. [11] measured a sensitivity of 2.0×10^{-10} at the nineth fractional Talbot distance at 24.9 keV. More recently, Schulz et al. [16] measured a sensitivity of 2.3×10^{-10} at the ninth fractional Talbot distance at 23 keV. Note that the photon energies used for these studies were substantially lower than in the present case.

Figure 5 (online color at: www.pss-a.com) (a) Profile extracted from the pseudo-absorption tomogram. (b) Profile extracted from the phase tomogram. The letter "b" indicates the background: the immersion liquid.

indicated with dashed lines in Fig. 2(a). In the absorption profile, the edge-enhancement peaks are clearly visible.

5 Conclusions The present study demonstrates the quantitative correctness of the refractive index values retrieved by interferometric phase tomography. It also shows the superior contrast-to-noise ratio of the phase tomograms with respect to absorption images. Nonetheless, the absorption signal contained in the interferometric data remains a valuable source of complementary information.

We have demonstrated, through simulations based on segmented experimental data, that in the phase tomograms, stripe artifacts tangential to interfaces showing strong contrast are entirely caused by the phase wrapping phenomenon. The fact that these artifacts can be completely reproduced by simulations indicates that algorithms may be developed to eliminate these artifacts from interferometric tomography data.

In the configuration used in this experiment, with the two-grating setup operated at 35 keV in the fifth fractional Talbot order on a third-generation synchrotron, the refractive index resolution, with a detector pixel size of 8 μm, was 3.4×10^{-10}, expressed in terms of the standard deviation of the real part of refractive index. The fact that this value is not quite as good as values reported in other studies is most likely influenced by the higher photon energy used here and by the presence of phase-wrapping artifacts generated by sample features showing strong contrast. These artifacts extend into other regions of the image.

These results confirm that grating interferometry with monochromatic synchrotron radiation can be a useful tool for high-accuracy measurements of the refractive index with applications in biological science, materials science, and also fundamental physics.

References

[1] R. Fitzgerald, Phys. Today **53**(7), 23–27 (2000).

[2] A. Momose, Jpn. J. Appl. Phys. **44**, 6355–6367 (2005).

[3] C. David, B. Nöhammer, H. H. Solak, and E. Ziegler, Appl. Phys. Lett. **81**, 3287–3289 (2002).

[4] A. Momose, S. Kawamoto, I. Koyama, Y. Hamaishi, K. Takai, and Y. Suzuki, Jpn. J. Appl. Phys. **42** (Part 2, No. 7B), L866–L868 (2003).

[5] F. Pfeiffer, T. Weitkamp, O. Bunk, and C. David, Nature Phys. **2**, 258–261 (2006).

[6] T. Weitkamp, I. Zanette, C. David, J. Baruchel, M. Bech, P. Bernard, H. Deyhle, T. Donath, J. Kenntner, S. Lang, J. Mohr, B. Müller, F. Pfeiffer, E. Reznikova, S. Rutishauser, G. Schulz, A. Tapfer, and J. P. Valade, in: Developments in X-ray Tomography VII, edited by S. R. Stock, Proc. SPIE, Vol. 7804 (SPIE, Bellingham, WA, USA, 2010), p. 780406.

[7] T. Weitkamp, P. Tafforeau, E. Boller, P. Cloetens, J. P. Valade, P. Bernard, F. Peyrin, W. Ludwig, L. Helfen, and J. Baruchel, in: X-ray Optics and Microanalysis: Proceedings of the 20th International Congress, edited by M. Denecke and C. T. Walker, AIP Conf. Proc., Vol. 1221 (AIP, Melville, NY, USA, 2010), pp. 33–38.

[8] J. Herzen, T. Donath, F. Pfeiffer, O. Bunk, C. Padeste, F. Beckmann, A. Schreyer, and C. David, Opt. Express **17**(12), 10010–10018 (2009).

[9] J. Zambelli, N. Bevins, Z. Qi, and G. H. Chen, Med. Phys. **37**(6), 2473–2479 (2010).

[10] T. Weitkamp, A. Diaz, C. David, F. Pfeiffer, M. Stampanoni, P. Cloetens, and E. Ziegler, Opt. Express **13**, 6296–6304 (2005).

[11] F. Pfeiffer, O. Bunk, C. Kottler, C. Grünzweig, C. David, M. Bech, G. Le Duc, A. Bravin, and P. Cloetens, Phys. Med. Biol. **52**, 6923–6930 (2007).

[12] C. David, J. Bruder, T. Rohbeck, C. Grünzweig, C. Kottler, A. Diaz, O. Bunk, and F. Pfeiffer, Microelectron. Eng. **84**, 1172–1177 (2007).

[13] E. Reznikova, J. Mohr, M. Börner, V. Nazmov, and P. J. Jakobs, Microsyst. Technol. **14**, 1683–1688 (2008).

[14] M. Sanchez del Rio, and R. J. Dejus, in: Advances in Computational Methods for X-ray and Neutron Optics, edited by M. Sanchez del Rio, Proc. SPIE, Vol. 5536 (SPIE, Bellingham, WA, USA, 2004), pp. 171–174.

[15] D. C. Ghiglia and M. D. Pritt, Two-Dimensional Phase Unwrapping: Theory, Algorithms, and Software (Wiley, New York, 1998).

[16] G. Schulz, T. Weitkamp, I. Zanette, F. Pfeiffer, F. Beckmann, C. David, S. Rutishauser, E. Reznikova, and B. Müller, J. R. Soc. Interface **7**(53), 1665–1676 (2010).